Atomic resolution structures of key enzyme MCR in anaerobic methanotrophy reveal novel and extensive post-translational modifications.

Marie-C. Müller[1], Martijn Wissink[2], Priyadarshini Mukherjee[1], Nicole von Possel[1], Rafael Laso-Pérez[7,8], Sylvain Engilberge[3,4], Philippe Carpentier[5], Jörg Kahnt[6], Gunter Wegener[7], Cornelia U. Welte[2], Tristan Wagner[1,4#]

[1] Microbial Metabolism research group, Max-Planck-Institute for Marine Microbiology, Celsiusstraße 1, 28359 Bremen, Germany

[2] Department of Microbiology, Radboud Institute for Biological and Environmental Sciences (RIBES), Radboud University, Heyendaalseweg 135, 6525 AJ Nijmegen, The Netherlands.

[3] European Synchrotron Radiation Facility, 38043 Grenoble, France

[4] Univ. Grenoble Alpes, CEA, CNRS, Institut de Biologie Structurale, 38044 Grenoble, France.

[5] Univ. Grenoble Alpes CEA CNRS, IRIG-LCBM UMR 5249, 38000 Grenoble, France.

[6] Max Planck Institute for Terrestrial Microbiology, Karl-von-Frisch-Strasse 10, 35043 Marburg, Germany

[7] HGF MPG Joint Research Group for Deep-Sea Ecology and Technology, Max-Planck-Institute for Marine Microbiology, Celsiusstraße 1, 28359 Bremen, Germany

[8] Systems Biology Department, Centro Nacional de Biotecnología (CNB-CSIC), Madrid, Spain.

[#]Correspondence: twagner@mpi-bremen.de

Abstract

Anaerobic methanotrophic archaea (ANME) are crucial to planetary carbon cycling. They oxidise methane in anoxic niches by transferring electrons directly to nitrate or metal oxides and alternatively to sulfate-reducing bacteria. Due to their physiological complexity, none of the ANME species have been isolated, hampering the biochemical investigation of the enzymatic processes involved in anaerobic methane oxidation. Here, we deciphered the methane-capturing enzyme through native purification directly from microbial enrichments. Freshwater ANME-2d reducing nitrate, grown in bioreactors, and marine microbial enrichment containing ANME-2c, along with its bacterial syntrophic partners, were used as model systems. The crystal structures of the Methyl-Coenzyme M Reductases (MCRs), refined to true atomic resolution, captured its most precise image to date. Despite their physiological differences, these ANMEs have extremely conserved MCR structures, similar to homologs from methanogenic *Methanosarcinales,* rather than the phylogenetically distant MCR of ANME-1 isolated from Black Sea mats. An exceptional content of seven post-translational modifications was observed *in cristallo*. Among them was a novel 3(*S*)-methylhistidine on the γ-chain of the ANME-2d MCR. Krypton gassing did not lead to the detection of an internal channel that would facilitate alkane diffusion to the active site, contrary to the ethane-activating homologue. Our results corroborate that MCRs from freshwater ANME-2d and marine ANME-2c should follow the conserved radical reaction mechanism of the methane-generating counterpart. The described pattern of post-translational modifications, different to ANME-1, highlights the importance of native purification as an unbiased approach to discovering intrinsic enzymatic features in uncultivated microorganisms existing in nature.

45 Introduction

46 In light of climate change, studies about planetary methane fluxes have become increasingly
47 important due to the global impact of the greenhouse gas. In anoxic marine sediments, 71 % of
48 biogenic methane is transformed into the less potent greenhouse gas CO_2 through the process
49 of anaerobic oxidation of methane (AOM)(1). The same is true in terrestrial and freshwater
50 systems where AOM can account for up to 50 % reduction in methane emissions in
51 wetlands(2). The only microorganisms capable of performing AOM without the use of oxygen
52 as a methane-activating agent are anaerobic methanotrophic archaea (ANME)(3, 4). To date,
53 all ANMEs described so far have been found habiting marine systems at the exception of
54 ANME-2d(5, 6). Electrons retrieved over the complete methane oxidation to CO_2 can be
55 transferred to sulfate-reducing *Deltaproteobacteria*, most likely by direct interspecies electron
56 transfer (DIET) through nanowires(7, 8). Reports proposed that some ANMEs performed non-
57 syntrophic AOM by coupling methane oxidation to Fe(III) or Mn(IV) reduction in marine and
58 brackish environments(9). In addition, freshwater ANME-2d reduce nitrate(10) or can colonise
59 electrodes and generate electricity(11).

60 Despite their common ability to turn methane into CO_2, ANME-1 and ANME-2/ANME-3 are
61 phylogenetically far apart. To understand their physiological distinctions, it is of utter
62 importance to investigate the fundamental molecular mechanism of AOM. Despite extensive
63 efforts, the gathered biochemical information on ANMEs is scarce due to the absence of an
64 axenic culture. Nevertheless, some laboratories have succeeded in obtaining enrichments of
65 microbial consortia(12-14), a strenuous process due to the extremely low doubling times of
66 ANME. This achievement can represent a turning point in deciphering how microbes catabolise
67 methane and inspire biotechnological applications.

68 Methane activation, the first reaction in AOM, has been proposed to be carried out by the
69 Methyl-coenzyme M reductase (MCR). Accordingly, the reaction would follow the reverse
70 direction of methanogenesis(15). In the proposed mechanism, the heterodisulfide, made of
71 Coenzyme M (HS-CoM) and Coenzyme B (CoB-SH), would react with methane to generate
72 methyl-S-CoM and free CoB-SH through a radical mechanism catalysed by the Ni-containing
73 tetrapyrrole cofactor F_{430}(16, 17). Methane conversion to methyl-S-CoM was previously
74 proved in the methanogen *Methanothermobacter marburgensis*(18) despite its unfavourable
75 thermodynamics (Gibbs free energy change of +30 $kJ.mol^{-1}$ of transformed methane)(4). To
76 perform this difficult process, ANMEs produce considerable quantities of MCR, which
77 represents by far the most abundant cellular enzyme(15, 19, 20). In addition, a thermodynamic

78 pull allowing an immediate conversion of methyl-S-CoM should proceed, leading to
79 subsequent transformation to CO_2.

80 MCR consists of a dimer of heterotrimers $(\alpha\beta\gamma)_2$ harbouring the cofactor F_{430} in each active
81 site(17). The catalytic chamber and its close surroundings contain many post-translational
82 modifications (PTMs) that vary in different methanogens and are carried on the α-subunit. No
83 correlation has so far been observed between the PTMs and phylogeny. While the installation
84 machinery of some of them has been reported, their physiological functions remain elusive(21-
85 23). Structures of ten methanogenic MCRs have yielded considerable information, highlighting
86 conserved overall features(16, 24). In contrast, the unique MCR structure from ANME-1
87 revealed unique traits, including a modified methylthio-F_{430} cofactor, a cysteine-rich patch, and
88 two different PTMs (*i.e.*, a C7-hydroxy-tryptophan and a methionine sulfoxide)(25),
89 corroborated by biochemical studies(15, 19).

90 The unique traits hint towards the presence of other unexpected features in ANME MCRs.
91 Acquiring snapshots of the phylogenetically different counterparts in ANME-2/ANME-3
92 would stimulate applied research in methane mitigation. Attempts have been made to facilitate
93 structural studies of ANME MCRs, including successful recombinant expression of ANME-1
94 MCR and the ethyl-CoM reductase specialised to activate ethane from '*Candidatus*
95 Ethanoperedens thermophilum'(26). However, this approach is biased as the machinery for
96 generating and installing native F_{430} variants, species-specific PTMs, and dedicated chaperones
97 required for correct folding are absent in the recombinant host. Moreover, artefactual chimeric
98 assemblies have been observed between the native MCR from the methanogenic host and the
99 recombinant ANME-2 MCR-γ. Similarly, the cultivation-independent approach of
100 computational protein structure modelling exhibits biases as the process is guided by extracted
101 data from known models but cannot predict the physiological cofactor, PTMs, and other
102 unknown traits such as water networks and gas channels. As an illustration, the structure of the
103 Ethyl-Coenzyme-M Reductase (ECR, proposed to catalyse the first reaction in anaerobic
104 ethane oxidation) harbours a dimethylated-F_{430} cofactor, a widened active site and unique
105 PTMs (N^2-methylhistidine and a 3-methylisoleucine) that scaffold a gas channel connecting
106 the active site to the solvent to favour alkane diffusion(20). Therefore, to explore the specific
107 features of alkane-capturing enzymes, the investigation of native systems still prevails, which
108 is a challenge in the case of non-isolated microbes such as ANMEs.

109 In this study, we purified MCRs directly from microbial enrichments dominated by ANME-2
110 and compared them to the ANME-1 structure. The native structures obtained at (sub)atomic
111 resolution depict the architecture of the methane-capturing enzyme, with the discovery of a
112 novel PTM on the γ-subunit. These findings expand the knowledge about this crucial enzyme
113 in these fascinating organisms, highlighting the importance of studying the natural microbial
114 diversity.

115

116 ## Results

117 **Isolation of the core catabolic enzyme MCR from marine and freshwater ANME-2**

118 Cultures containing high enrichments of ANME are rare due to the laborious enrichment
119 procedures and the long division time of these organisms. Successive breakthroughs in the
120 cultivation of ANME-2 species have allowed us to access marine and freshwater
121 representatives to study differences among their MCRs through native protein purification
122 (Figure 1 and Supplementary Fig. S1). In all presented cases, the native protein isolation was
123 based on MCR tracking by following its intrinsic properties: the absorption signature from the
124 F_{430} cofactor and the typical pattern on denaturing gels (SDS-PAGE, Supplementary Fig. S2).

125 Investigations were started on a relatively simplified system in which ANME-2d grew
126 independent of sulfate-reducing partners. Biological samples were retrieved from Ooijpolder
127 (Netherlands)(27, 28), and Vercelli rice fields (Italy)(11, 14) and cultivated in bioreactors for
128 >5 years, significantly enriching ANME-2d with nitrate as electron acceptor. Metagenomic
129 analysis of the Ooijpolder enrichment samples showed a read-based relative abundance of 20-
130 40 % *Ca.* Methanoperedens(29) with main strain '*Ca*. Methanoperedens' BLZ2(30) (further
131 referred to as ANME-2d^{O}).

132 In comparison, metagenomic analysis of the Vercelli rice field enrichment sample showed a
133 read-based relative abundance of 15 % '*Ca*. Methanoperedens', with main strain '*Ca*.
134 Methanoperedens' Vercelli Strain 1(31) (further referred to as ANME-2d^{V}). Both samples were
135 separately processed for protein purification, starting from 17.5 g and 12.5 g of ANME-2d^{O}
136 and ANME-2d^{v} containing biomass and yielding 114 mg and 14 mg of the major MCR,
137 respectively (Figure 1).

138 Furthermore, the purification setup was tested on microbial enrichment from a marine system.
139 Here, material was sampled at Amon Mud Volcano in the Mediterranean Sea at a depth of

140 1,120 m and a temperature of 14 °C. The microbial enrichment, grown at 20 °C in batch serum
141 bottles since 2003, gathered mostly ANME-2a/b and ANME-2c species and their microbial
142 partners Seep-SRB1 and Seep-SRB2 based on 16S rRNA gene sequencing(7)(Supplementary
143 Fig. S1). The limited processed biomass of 3.21 g contained the microbial mixture as well as
144 inorganic particles, and a final quantity of 4.9 mg of the major MCR could be extracted.

145 In all cases, the final purified MCR fractions subjected to UV/Vis spectroscopy presented a
146 peak at 425 nm due to the F_{430} cofactor in accordance with previous reports for methanogenic
147 MCRs (Supplementary Fig. S2b-c)(20, 32). While the final SDS-PAGE suggests a high sample
148 homogeneity in solution, we could not exclude a mixture of MCRs from different subspecies.
149 Therefore, we used the selective crystallisation process to isolate and identify a single variant
150 by X-ray crystallography.

151

152 **MCR shows a well-conserved overall architecture**

153 All MCR samples crystallised in a relatively short time (i.e., less than a week), which was
154 unexpected based on the heterogeneity. X-ray diffraction data was collected, and models were
155 refined to a final resolution of 0.98 and 0.94 Å (Table 1) for the MCR from ANME-2d^{O} and
156 ANME-2d^{V}, respectively. Both MCRs crystallised in a monoclinic space group with similar
157 unit cell dimensions. Despite the differences in the organisms and the slight deviations in the
158 crystallisation solution (see methods), both MCR models shared the same crystalline packing
159 (Supplementary Fig. S3). This suggests a very close sequence identity that would maintain the
160 contacts on the surface to establish the same crystal lattice. This was confirmed after
161 sequencing the MCR from the initial electron density following the molecular replacement,
162 presenting an average deviation of only 3-5 % in sequence identity (*i.e.*, with an amino acid
163 sequence identity of 95.4, 97.2, and 95.6 % for α, β, and γ, respectively), resulting in an almost
164 identical structural superposition (root mean square deviations (rmsd) of 0.09 Å with an overall
165 of 2,186 aligned Cα).

166 The dataset obtained for the ANME-2c enrichment was also of sufficiently high quality to
167 unequivocally determine the sequence from the electron density map of the initial model,
168 refined to a resolution of 1.34 Å. The derived sequence perfectly matched the one of ANME-
169 2c MCR from the metagenomic data (Supplementary Fig. S4). Based on the crystal structure,
170 MCR from ANME-2c seems to form stable dimers (Supplementary Fig. S3), as pointed out by
171 the PISA server analyses (the dimer exhibiting a ΔG^{int} of −617.2 kcal.mol^{-1} and a ΔG^{diss} of

172 26.8 kcal.mol^{-1}, with analyses performed on the 25th of November 2024). The dimeric interface
173 is exclusively formed by the interaction of the α-subunits presenting many interactions with
174 the C-terminal extension. The dimeric state does not disturb the access to the active site. Due
175 to the low quantities of MCR obtained at the end of the purification and the slow growth of the
176 consortium, we could not test if this dimeric arrangement reflects a crystallisation artefact or a
177 stable entity in solution, and more studies will have to be carried out. On the other hand, the
178 predicted trimeric arrangement of the MCR from ANME-2d^{O} observed in blue native
179 PAGE(30) was not detected in the crystal structure. Nevertheless, we cannot exclude that the
180 purification and crystallisation process might have disrupted a trimeric organisation.

181 Despite the different environmental niches, the marine ANME-2c and freshwater ANME-2d
182 derived MCR share relatively high amino acid sequence identity (*i.e.*, with an identity of 63.6,
183 61.5, and 71.4 % for α, β, and γ, respectively, based on MCR from ANME-2d^{V}, Supplementary
184 Fig. S5-6). The three MCRs from ANME-2 share a matching overall structure with previously
185 structurally studied methanogenic MCRs as well as the methanotrophic ANME-1 MCR and
186 ECR from *Ca.* E. thermophilum (Figure 2, Supplementary Fig. S5-6), the closest homolog
187 being the MCR from *Methermicoccus shengliensis*(32). Besides the overall similarity,
188 structural differences are notable and summarised in Figure 2. The electrostatic profile of the
189 surface is also similar to previously studied MCRs, with both ANME-2d members exhibiting
190 more pronounced positive charges at the entrance leading to the active site than a typical
191 methanogenic MCR (Supplementary Fig. S7).

192

193 **A sealed, strictly conserved catalytic chamber is covered by seven post-translational**
194 **modifications**

195 The active site of the three ANME-2 MCRs is highly conserved with the described MCRs from
196 methanogenic archaea and contains a canonical F_{430} cofactor in accordance with previous
197 studies(19) (Fig. 3, Supplementary Fig. S8). The subatomic resolution of both ANME-2d
198 structures allows the visualisation of the majority of hydrogen atoms and depicts the accurate
199 position of each atom of the ligands. Both MCRs from ANME-2c and ANME-2d^{O} contain
200 reduced coenzymes trapped in the active site. However, MCR from ANME-2d^{V} exhibits a
201 mixture of reduced and oxidised coenzymes (i.e., heterodisulfide). The ligand coordinating
202 residues are almost perfectly conserved (Fig. 3a-b, Supplementary Fig. S9).

203 The discovery of a gas channel in the ethane-capturing enzyme motivated us to explore whether
204 ANME-2 MCR has a similar accession system for methane. Analysis of the internal cavities in
205 all three models revealed tunnels protruding from the active site with small diameters
206 comparable to the methanogenic counterparts (Supplementary Fig. S10). Their positions and
207 diameters differ from those of the ECR from *Ca.* E. thermophilum. Therefore, we used Krypton
208 instead of Xenon to mimic the sterical hindrance of methane and performed high-pressure
209 gassing for a few minutes on the MCR of ANME-2c, which presented one of the largest
210 protrusions. Based on the anomalous signal of the dataset collected at the Krypton K-edge, no
211 signals were observed in the active site or tracking in a hydrophobic tunnel (Fig. 3c,
212 Supplementary Fig. S11). Krypton atoms are rather positioned on the outer shell of the protein,
213 trapped in hydrophobic pockets, as previously observed for the methanogenic enzyme from *M.*
214 *marburgensis*(20, 33). The absence of a dedicated gas tunnel reinforces the proposed scenario
215 that only ethane-specialized enzymes evolved this strategy through the introduction of loop
216 extensions and dedicated PTMs.

217 In the case of the three ANME-2 MCRs, a surprising number of seven PTMs were observed in
218 the electron density (Fig. 4, Supplementary Fig. S12 and S13). ANME-2c MCR includes the
219 conserved N^1-methylhistidine and thioglycine, as well as the common 5(*S*)-methylarginine,
220 2(*S*)-methylglutamine, and the rarer S-methylcysteine, didehydro-aspartate and 6-
221 hydroxytryptophane. The same PTMs are present in both ANME-2d MCRs, with the exception
222 of 2(*S*)-methylglutamine. Instead, the histidine 159 from the γ chain harbours a methyl group
223 on its β-carbon in a *S* configuration (i.e., 3(*S*)-methylhistidine). The histidine is highly
224 conserved and positioned at a distance of 3.5 Å to the F_{430} cofactor, with atom ND1 forming a
225 hydrogen bond to F_{430}. However, the modified methyl group is distanced at ~5.7 Å and directed
226 away from the cofactor without disturbing the positioning of surrounding residues
227 (Supplementary Fig. S14).

228

229 ## Discussion

230 Anaerobic methanotrophic archaea have a major effect on the global carbon cycle due to their
231 important role as a biological methane filter. The efficiency of their catabolism could be
232 employed in microbial-driven technology, as illustrated by ANME-2d producing an electrical
233 current from methane oxidation when grown on electrodes(11) or methane sink in
234 wastewater(34). Therefore, efforts are carried by the scientific community to decipher their

235 metabolisms and find out why some MCRs are specialized into methane capture rather than
236 generation. Here, by directly exploiting microbial consortia, we isolated and structurally
237 characterised the catabolic enzymes from ANME representatives, expanding the available pool
238 of methanotrophic MCR structural models from one to four, and offering prospect in the
239 mechanistic of methane activation.

240 Compared to active MCR retrieved from hydrogenotrophic methanogens, it is currently not
241 feasible to obtain reactivated ANME enzymes. Still, our structural insights showed that
242 compared to the ECR system from *Ca.* E. thermophilum (belonging to a sister group of ANME-
243 2d), no specific gas channels connecting the core of the enzyme to its surface could be
244 detectable by Kr pressurization. This confirms that while the enzyme closure upon
245 heterodisulfide binding still allows ethane diffusion in ECR, the methane specialized enzyme
246 should first trapped methane in the catalytic chamber(16), a mechanistic that should be shared
247 among ANME MCRs.

248 Structural differences exist between MCR from ANME-2 and ANME-1 isolated from Black
249 Sea mats that are more likely linked to taxonomy than to adaptation to ecological niches, as
250 illustrated by the MCRs from freshwater and marine anaerobic methanotrophic archaea
251 investigated in this study. Based on proposed evolutionary scenario supporting that
252 methanotrophy in ANME-1 originates from alkanotrophy, while it rather evolved from
253 methanogenesis in *Methanosarcinales* (e.g., ANME-2)(35), the perceived structural
254 organization of MCR from both clades are most likely a result of convergent evolution rather
255 than sharing the same evolutionary basis. Behind the differences in cofactors (e.g., methylthio-
256 F_{430} versus classic F_{430}) and structural particularities (e.g., presence or absence of a cysteine-
257 rich path), the PTM gallery are divergent (Supplementary Fig. S13) except from three structural
258 positions that seem to be of importance for methanotrophy: the conserved N^1-methylhistidine
259 and thioglycine, and the 5(*S*)-methylarginine in ANME-2/methanogens compensated by S-
260 oxymethionine/7-hydroxy-L-tryptophan in ANME-1.

261 With seven PTMs, ANME-2 MCRs gather the most complete repertoire of modifications
262 reported across methanogens, which is contrasting with its closest structural relative, *M.*
263 *shengliensis*(36) belonging to the same order, harbouring the most reduced gallery with three
264 PTMs. A rational explanation for the extravagant large number of PTMs would be the kinetic
265 limitation of methane activation compared to methane release reaction. Indeed, when
266 considering the appK_m value of ≈10 mM obtained from the MCR isoform I of

267 *Methanothermobacter marburgensis*, then the catalytic rates of ANME MCRs would be
268 restricted under physiological conditions where methane would be lower than the mM. If, as
269 postulated by other groups(22, 23), PTMs stabilise the active site and ligands, it might be
270 beneficial for the microbe to invest in equipping its core catabolic machinery to enhance, even
271 slightly, its kinetic properties (i.e., by further decreasing the appK_m). Further studies of other
272 ANME MCRs will be necessary to observe a correlation between the increased PTM amount
273 and methanotrophy. On the same line, future studies could investigate how common the 3(*S*)-
274 methylhistidine is and if it exists in other *Methanosarcinales*. To our knowledge, this is the
275 first report of a 3(*S*)-methylhistidine in a natural protein and the first PTM identified on the γ-
276 chain of any characterised MCR. While the methylation occurs on a residue coordinating the
277 F_{430} cofactor, it appears to have no immediate effect on the surrounding active site, raising
278 questions about its role, in line with the so far mostly unresolved functions of the majority of
279 PTMs observed in MCRs(16, 24). However, since all crystallographic structures are mere
280 snapshots of a single state, we cannot exclude a role during catalysis or enzyme assembly.
281 Located on a loop at the surface of the γ-subunit, the 3(*S*)-methylhistidine could be installed
282 before the oligomeric assembly by a dedicated methyl-transferase. Due to the low
283 nucleophilicity of the β-carbon, the reaction should occur similarly to the installation of a
284 methylarginine (installed by the Mmp10 methyltransferase(23)) or methylglutamine rather
285 than the N^1-methylhistidine in which an S-adenosylmethionine dependent methyltransferase
286 would substitute a hydrogen of the imidazole ring nitrogen with a methyl group. ANME-2d
287 encodes an Mmp10 homolog upstream of the MCR operon that could potentially fill the role.

288 The sub-atomic resolution datasets, detailing the active site, cofactor, and coenzymes to
289 unprecedented levels, represent an important step for future studies in understanding the
290 molecular mechanisms of methane activation. For instance, assigning protonation states of
291 active site residues accessible by Neutron diffraction would be an important asset. Moreover,
292 with its high yield/high purity, rapid micro-crystal formation and excellent diffraction quality,
293 MCR of ANME-2d$^{O/V}$ are well suited for time-resolved crystallography.

294 By delivering these accurate models, our work emphasises the need to understand how the
295 native systems operate through an unbiased approach. Highlighting which type of cofactor
296 should be inserted or which PTMs would be appropriate to install would guide the design of
297 efficient heterologous methane capture systems for mitigating greenhouse gas emissions and
298 moving towards a zero-carbon emission society.

299

Material and Methods

Biomass acquisition and microbial enrichments.

ANME-2c cultivation: Sediment was sampled by multicore at Amon Mud Volcano, Nile deep-sea fan, Mediterranean Sea at 032° 21.70 N, 031° 23.40 E at a water depth of 1,120 m and 14 °C with the research vessel RV L'Atalante NAUTINIL cruise in 2003. Onboard samples were transferred into gas-tight bottles. In the home laboratory, sediment slurries were set up with a synthetic marine sulfate reducer medium at pH 7.4 (Widdel and Bak, 1992(37)) and methane headspace at 20 °C. Incubated slurries showed methane-dependent sulfate reduction within a few days. To remove sediment debris, cultures were continuously incubated with methane as the sole electron donor and sulfate as the electron acceptor. The activity-based doubling time for both cultures, monitored by sulfide measurements, was about 4-6 months. Consecutive dilution and further incubation resulted in debris-free cultures of detached flocks essentially composed of AOM-performing methane-oxidizing archaea and sulfate-reducing bacteria consortia. For more detailed cultivation methods, see Laso-Pérez *et al*., 2018(38).

ANME-2d^{O} bioreactor cultivation from Ooijpolder sample: Granular biomass was obtained from a highly enriched bioreactor culture(30). The culture was maintained in an anaerobic 15 L sequencing fed-batch reactor (30 °C, pH 7.3 ± 0.1 controlled with $KHCO_3$, stirred at 200 rpm, with a working volume between 8 and 11 L). The reactor was continuously sparged with 15 mL.min^{-1} CH_4/CO_2 (95:5) and fed with medium (flow rate 2-2.5 L.day^{-1}), as described in Kurth *et al.* 2019(28). Medium contains nitrate (15-25 mM) with an adaptation of the KH_2PO_4 concentration to 0.05 g.L^{-1}. Once a day, the biomass settled for 5 min, after which the excess liquid in the reactor was pumped off to a volume of 8 L. Metagenome data from the time of sampling showed a read-based relative abundance of 20 – 40 % '*Ca*. Methanoperedens'(29), with as main strain '*Ca*. Methanoperedens BLZ2'(30) and nearly 50 different bacterial species(28).

ANME-2d^{V} bioreactor cultivation from Vercelli rice fields sample: Granular biomass was obtained from a freshwater N-DAMO bioreactor enrichment culture first described by Vaksmaa *et al.* 2017(14). The culture was maintained in an anaerobic 15 L sequencing-fed batch reactor (room temperature, pH 7.3 ± 0.1 controlled with $KHCO_3$, stirred at 200 rpm) with a working volume between 8 and 11 L. The reactor was continuously sparged with 10 mL.min^{-1} CH_4/CO_2 (95:5) and fed with medium (flow rate 1.5-2 L.day^{-1}) containing sodium nitrate (5-8

331 mM). Once a day, the biomass settled for 5 min, after which the excess liquid in the reactor
332 was pumped off to a volume of 8 L.

333 The medium contained 0.07 $g.L^{-1}$ $MgSO_4.7H_2O$, 0.1 $g.L^{-1}$ $CaCl_2.2H_2O$, 0.05 $g.L^{-1}$ K_2HPO_4,
334 0.5 $mL.L^{-1}$ of trace element solution, 0.3 mL iron solution (54 $g.L^{-1}$ $FeCl_3.6H_2O$ and 114.6
335 $g.L^{-1}$ nitrilotriacetic acid), and 0.1 $mL.L^{-1}$ of Wolin's vitamin solution (DSMZ 141). The trace
336 element solution contained per liter: 0.12 g $CeCl_3.7H_2O$, 0.6 g $CoCl_2.6H_2O$, 4.0 g $CuSO_4$, 0.07
337 g H_3BO_3, 1.0 g $MnCl_2.4H_2O$, 0.35 g $Na_3MoO_4.2H_2O$, 0.1 g $Na2WO_4.2H_2O$, 0.95 g
338 $NiCl_2.6H_2O$, 0.14 g SeO_2, 1.44 g $ZnSO_4.7H_2O$.

339 **Metagenome sequencing**

340 ANME-2c: The metagenomic reads were assembled using SPAdes v. 4.0.0 with default
341 parameters (39). We performed automatic binning with the software SemiBin (v. 2.1.0) on the
342 *de novo* assembly using the *single_easy_bin* pipeline(40). We obtained three bins affiliated
343 with ANME-2 according to GTDB (v. 2.1.1) classification (41). We annotated them using
344 prokka v. 1.14.6(42), and extracted the corresponding MCR proteins.

345 ANME-2d: Genomes were retrieved from GTDB-Tk v2.4.0 for ANME-2D^O, '*Ca*.
346 Methanoperedens sp.' BLZ2 under accession number GCA_002487355.1 and ANME-2D^V,
347 '*Ca*. Methanoperedens' Vercelli Strain 1 under accession number GCA_905339155.1.

348 MCR sequences from '*Ca*. Methanoperedens sp.' BLZ2 correspond to WP_097300250.1,
349 WP_097300253.1, and WP_097300251.1 for the α, β, and γ subunits, respectively. MCR
350 sequences from '*Ca*. Methanoperedens' Vercelli Strain 1 correspond to MCX9030096.1,
351 MCX9030093.1, and MCX9030095.1, for the α, β, and γ subunits, respectively.

352 DNA extraction and sequencing of ANME-2d^O and ANME-2d^V were performed as described
353 in Wissink et al. 2024(29). Microbial taxonomic profiles of ANME enrichments were
354 determined using SingleM(43) against the GTDB-Tk database version 2.4.0. Read quality was
355 assessed using FASTQC v0.11.9. The ANME-2c sample consisted of 83 million reads of 150
356 bp, which resulted in a 2367× profile coverage, while the ANME-2d^O and ANME-2d^V samples
357 consisted of 6.6 and 5.5 million reads of 300 bp, respectively, resulting in 572× and 574×
358 profile coverage.

359 **Sample treatment and lysis**

360 ANME-2c: Two anaerobic 150 mL AOM enrichment cultures were used as starting material.
361 Particles were settled overnight at RT, followed by the removal of ~130 mL of clear
362 supernatant. H_2S in the culture headspace was replaced with N_2 gas before transfer to an
363 anaerobic chamber. Cell lysis and preparation of extracts were performed in a N_2/CO_2
364 atmosphere (90:10 %) at 31 °C. Both samples were pooled and centrifuged at 8,000 × *g* for 5
365 min. The supernatant was carefully removed, resulting in a pellet of ~ 3.21 g (wet weight). The
366 aggregates were resuspended in 30 mL IEC-A buffer (50 mM Tricine/NaOH pH 8 and 2 mM
367 dithiothreitol (DTT)) and lysed via two rounds of sonication interceded with a French Press
368 treatment at 1,000 PSI (6.895 MPa). The French press cell was flushed with N_2 gas before use
369 to ensure anoxic conditions. Unfortunately, 7.5 mL of the lysed sample was lost in the airlock
370 due to an accidental break of the serum flask. The leftover total extract was then diluted to 60
371 mL with IEC-A, followed by centrifugation at 45,000 × *g* for 30 min at 18 °C. 100 µL was
372 withdrawn at each step for SDS-PAGE analysis (Supplementary Fig. S2).

373 ANME-2d^{O}: Frozen biomass containing '*Ca.* Methanoperedens' BLZ2 (17.5 g of cells) was
374 transferred to an anaerobic chamber containing an N_2/CO_2 atmosphere (90:10 %) and
375 resuspended in 3x30 mL buffer IEC-A. Cells were first lysed via two rounds of sonication
376 (SONOPULSE Brandelin, 75 % power, 30 sec, 1st round: 4 cycles, 2nd round: 3 cycles)
377 interceded with a French Press treatment at 1,000 PSI (6.895 MPa). The French press cell was
378 previously flushed with N_2 to ensure anoxic conditions. After the second round of sonication,
379 the sample was centrifuged at 45,000 × *g* for 30 min at 18 °C. The supernatant was collected
380 and subjected to ultracentrifugation at 100,000 × *g* for 1.5 hours at 4 °C (rotor used: 70Ti,
381 Beckman Coulter). 100 µL of the total cell extract and soluble fraction were withdrawn for the
382 Bradford assay and SDS-PAGE.

383 ANME-2d^{V}: 12.47 g of frozen biomass was resuspended in 60 mL buffer IEC-A. Cells were
384 processed the same way as ANME-2d^{O} except for the following variation. The supernatant
385 from ultracentrifugation was sonicated for 4 extra cycles, and 40 mL of filtered supernatant
386 was obtained before injection on the HiTrap Q HP column.

387 **MCR purification**

388 ANME-2c: Protein purification was performed under anoxic conditions in an anaerobic Coy
389 tent with an N_2/H_2 atmosphere (97:3 %) at 20 °C under yellow light. Before every injection
390 onto a chromatography column, the sample was filtered using a 0.2 µm nitrocellulose filter
391 (Sartorius, Germany). Proteins were tracked via multi-wavelength absorbance monitoring (λ

392 280, 415 and 550 nm) in combination with SDS-PAGE. The 60 mL of filtered soluble extract
393 (20.7 mg protein) was loaded on a 1 mL HiTrap Q HP column equilibrated with IEC-A. The
394 proteins were eluted with a two-step protocol, reaching 0.5 M and then 1 M at a flow rate of
395 0.7 $mL.min^{-1}$. MCR was eluted at 0.5 M NaCl, and the pool (~13 mL) was diluted ~1:4 (protein
396 sample: buffer) with IEC-A buffer. The filtered sample was loaded on a 0.982 mL MonoQ
397 column. The elution was performed at a gradient of 100 to 700 mM NaCl at 0.5 $mL.min^{-1}$. The
398 pooled MCR fractions were diluted ~1:4 (protein sample: buffer) with HIC-B buffer (25 mM
399 Tricine/NaOH pH 7.6, 2 M $(NH_4)_2SO_4$, and 2 mM DTT). The pool was filtered and passed on
400 a 1.622 mL Source15ϕ column. Proteins were eluted by applying a gradient of 1.5 to 0 M
401 $(NH_4)_2SO_4$ at 0.6 $mL.min^{-1}$. The final MCR pool was washed by dilution (1:1000) with storage
402 buffer (25 mM Tris/HCl pH 7.6, 10 % v/v glycerol, and 2 mM DTT) using a 30 kDa cut-off
403 concentrator to remove salts. Finally, the sample was concentrated to 200 µL. The protein
404 concentration estimated via the Bradford method was 24.6 $mg.mL^{-1}$. Purification with three
405 chromatography steps yielded a pure MCR fraction displaying the typical three-subunit pattern
406 on SDS-PAGE with molecular weights of ~65, 39, and 34 kDa (Supplementary Fig. S2).

407 ANME-2d^{O}: Purification was performed under the previously described conditions, and
408 fractions of interest were followed at λ 280. The soluble extract (90 mL at 7.82 $mg.mL^{-1}$) could
409 not be filtered due to the large particulate size and was directly injected into the 10 mL HiTrap
410 Q HP column pre-equilibrated with IEC-A buffer. After washing the column, the elution was
411 performed with a gradient of 0 to 650 mM NaCl for 10 column volumes (CV) at a 2 $mL.min^{-1}$
412 flow rate. The pool of interest was diluted 1:1 with HIC-B buffer, filtered, and loaded on the
413 1.622 mL Source 15ϕ column. A gradient from 80 % to 0 % $(NH_4)_2SO_4$ for 10 CV at a 1.5
414 $mL.min^{-1}$ flow rate was applied. The final MCR fractions were pooled and concentrated on a
415 Vivaspin centrifugation concentrator with a cut-off of 30 kDa. The buffer was exchanged by
416 ultrafiltration for the storage buffer (25 mM Tris/HCl pH 8.0, 10% v/v glycerol, 2 mM DTT,
417 and 100 mM NaCl) containing NaCl to prevent the spontaneous formation of microcrystals.
418 Around 2 mL of purified MCR were recovered at 57 $mg.mL^{-1}$, aliquoted into 50 µL, and stored
419 at 4 and −80 °C.

420 ANME-2d^{V}: Purification was performed under the previously described conditions, and
421 fractions of interest were followed at λ 280. The filtered soluble extract (40 mL) was injected
422 into the 10 mL HiTrap Q HP column pre-equilibrated with IEC-A buffer. After washing the
423 column, the elution was performed with a gradient of 0 to 650 mM NaCl for 16 column volumes
424 (CV) at a 2 $mL.min^{-1}$ flow rate. The pool of interest was diluted 1:2 (protein sample: buffer)

425 with HIC-B buffer, filtered, and loaded on a 5 ml HP Phenyl Sepharose column. A gradient
426 from 1.3 M to 0 M of $(NH_4)_2SO_4$ for 12 CV at a 1.0 mL.min^{-1} flow rate was applied. The final
427 MCR fractions were pooled and concentrated on a Vivaspin centrifugation concentrator with a
428 cut-off of 30 kDa. Ultrafiltration exchanged the buffer for storage buffer. Around 0.35 mL of
429 purified MCR were recovered at 40 mg.mL^{-1} and stored at 4 and −80 °C.

430 **UV-visible spectrophotometry**

431 UV-visible absorption spectra were recorded with a Cary 60 (Agilent Technologies)
432 spectrophotometer on a TrayCell with a 1 mm path.

433 **Phylogeny analyses**

434 We concatenated the three MCR subunits from each MAG and used them to calculate a
435 phylogenetic tree, including the sequences of the crystallised MCRs from ANME-2c and
436 ANME-2d of this manuscript and the sequences of previously crystallised MCRs. The
437 concatenated MCR sequences were aligned using MUSCLE v3.8.1551(44). The aligned
438 concatenated sequences were used to calculate a phylogenetic tree with RAxML v.8.2.12(45)
439 using a partition file to calculate differential models for each gene and the following parameters
440 '-m PROTGAMMAAUTO -f a -N autoMRE -k'.

441 **Crystallisation**

442 <u>ANME-2c:</u> The fresh preparation of MCR was immediately crystallised. Crystals were
443 obtained using the sitting drop method on 96-Well MRC 2-Drop Crystallization Plates in
444 polystyrene (SWISSCI, Switzerland), containing 90 µL of crystallisation solution in the
445 reservoir: 0.5 µL protein sample with 0.5 µL crystallisation solution were spotted. The
446 crystallisation was performed under anaerobic conditions via an OryxNano (Douglas
447 Instrument, UK) at 18 °C in a tent filled with 100 % N_2. Then, plates were transferred in a Coy
448 tent (N_2/H_2 atmosphere 97:3 %) at 20 °C. Crystals were formed following the first 24 hours.

449 The most successful condition (30 % v/v 2-Methyl-2,4-pentanediol, 100 mM Tris pH 8, 500
450 mM NaCl and 8 % w/v Polyethylene glycol 8,000) was replicated on a Junior Clover plate
451 (Jena Bioscience, Germany) under oxic conditions with 90 µL of the crystallisation solution in
452 the reservoir and 2 µL protein sample with 2 µL crystallisation solution in the well. Crystals
453 with yellow square or rectangular morphology appeared over the next two weeks.

454 ANME-2d^{O}: Following an initial screening on a 96-well MRC 2-Drop Crystallization Plates in
455 polystyrene done oxically at 18 °C, MCR crystals were reproduced using the sitting drop
456 method on the Junior Clover plate. The best crystals were obtained with a reservoir filled with
457 100 µL of the following crystallisation condition: 20 % w/v polyethylene glycol 3,350, 50 mM
458 Tris pH 8.0 and 200 mM potassium nitrate and by spotting 5 µL protein at a concentration of
459 2.19 mg.mL^{-1} with 2 µL crystallisation solution. Thick yellow brick-shaped crystals appeared
460 within 24-48 hours.

461 ANME-2d^{V}: Following an initial screening on a 96-well MRC 2-Drop Crystallization Plates in
462 polystyrene done oxically at 18 °C, MCR crystals were reproduced using the sitting drop
463 method on the Junior Clover plate. Here, the reservoir was filled with 100 µl of 20 % w/v
464 Polyethylene glycol 3,350 and 200 mM sodium thiocyanate pH 6.9, and the crystallisation well
465 contained 3 µL protein at a concentration of 40 mg.mL^{-1} with 2 µL mother liquor.

466 **Kr pressurisation**

467 ANME-2c MCR in solution was shipped to the High-Pressure Freezing Laboratory for
468 Macromolecular Crystallography (HPMX)(46) of the European Synchrotron Radiation Facility
469 (ESRF). The best crystallisation hit was repeated, and the crystals obtained were used for the
470 Krypton-pressurization experiment. Here, crystals were pressurised at 214 bars Krypton for 2
471 min before flash freezing in liquid nitrogen. X-ray crystallographic data were collected on
472 ID23-1 at 14.4 KeV, close to the Krypton fluorescence K-edge.

473 **X-ray data collection, processing, modelling and validation.**

474 MCR crystals were soaked in the crystallisation solution supplemented with 20 % v/v glycerol
475 for ANME-2d^{O} and 20 % v/v ethylene glycol for ANME-2d^{V} for 5-10 seconds before being
476 transferred to liquid nitrogen.

477 X-ray diffraction for ANME-2c crystals was collected at SOLEIL (Optimized Light Source of
478 Intermediate Energy to LURE) synchrotron, Saint-Aubin, France, at the beamline PROXIMA-
479 1. Crystals for both ANME-2d were collected at the European Synchrotron Radiation Facility
480 (ESRF), Grenoble, France, on the beamline BM07-FIP2.

481 The datasets were processed and scaled with *autoPROC* (Version 1.0.5, Global Phasing
482 Limited, Cambridge, UK)(47), except for the Krypton gassed sample that was integrated with
483 XDS and scaled with aimless from the CCP4 package. The structures were solved by molecular
484 replacement with *PHASER* from the *PHENIX* package (Version 1.19.2-4158)(48). For

485 molecular replacement, we used an AlphaFold 2(49) model based on the metagenome derived
486 amino acid sequence for MCR of ANME-2c, then the ANME-2c MCR model for ANME-2d^{O}
487 MCR and finally, the ANME-2d^{O} MCR model was used for molecular replacement for ANME-
488 2d^{V} MCR.

489 All models were then refined with *COOT* (Version 0.8.9.2)(50) and *PHENIX* refine. Because
490 of the high resolution, all atoms were considered anisotropic (except for the Krypton-pressured
491 structure), and hydrogens in riding mode were added. Since only anomalous data were
492 interesting for the Krypton-gassed crystal, a rigid body, followed by three cycles of *PHENIX*
493 refine, was performed to generate Fig. 3c and Supplementary Fig. S11. The models were
494 validated by the MolProbity server (http://molprobity.biochem.duke.edu). Figures of MCR
495 structures were generated with PyMOL (V. 2.2.0, Schrödinger, LLC). Sequence alignments
496 were generated with MAFFT 7(51) and visualised with ESPript 3.0(52). All models from Table
497 1 have only hydrogens modelled on the protein (*e.g.*, not on ligands and solvents). Internal
498 channels connecting the active site to the surface were generated by Caver(53).

499

500 Acknowledgements

501 We are thankful to the Max Planck Institute for Marine Microbiology and the Max Planck
502 Society for their continuous support. We thank Christina Probian and Ramona Appel of the
503 Microbial Metabolism laboratory for their continuous support. We acknowledge the SOLEIL
504 and ESRF synchrotrons for beam time allocation and the beamline staff of Proxima-1, ID23-1
505 and BM07-FIP-2. T.W. was supported by a European Research Council consolidator grant
506 [Grant number 101125699] and the Max Planck Society. The initial crystallisation screening
507 performed by an OryxNano robot was financed by the DFG priority programme 1927 Iron-
508 Sulphur for Life [Grant number WA 4053/1-1]. C.W. thankfully acknowledges financial
509 support from the Dutch Science Foundation through an NWO-VIDI Talent Grant [Grant
510 number VI.Vidi.223.012] and the SIAM Gravitation Grant [Grant number 024.002.002].

511

512 Author contributions

513 Enrichment of ANME-2c was done by G.W., enrichments of ANME-2d were done by M.W.
514 and C.W. Treatment of metagenomic data for ANME-2c and ANME-2d was done by R.L. and
515 M.W., respectively. Purification and crystallisation of ANME-2c MCR were performed by M.-

516 C.M. and N.v.P, purification and crystallisation of ANME-2d^{O} MCR was done by P.M. and
517 M.W., purification and crystallisation of ANME-2d^{V} were done by M.W. and T.W., data
518 collection was done by S.E, and T.W. X-ray data processing, model refinement and analysis
519 were done by M.-C.M. *in cristallo* spectrophotometry and Kr pressurisation were done by S.E.
520 and P.C. The manuscript was written by M.-C.M. and T.W. Manuscript edition and correction
521 was done by all authors.

522

523 References

524 1. Gao YH, Wang Y, Lee HS, Jin PK. Significance of anaerobic oxidation of methane
525 (AOM) in mitigating methane emission from major natural and anthropogenic sources: a
526 review of AOM rates in recent publications. Environ Sci Adv. 2022;1(4):401-25.
527 2. Segarra KE, Schubotz F, Samarkin V, Yoshinaga MY, Hinrichs KU, Joye SB. High
528 rates of anaerobic methane oxidation in freshwater wetlands reduce potential atmospheric
529 methane emissions. Nat Commun. 2015;6:7477.
530 3. Boetius A, Ravenschlag K, Schubert CJ, Rickert D, Widdel F, Gieseke A, et al. A
531 marine microbial consortium apparently mediating anaerobic oxidation of methane. Nature.
532 2000;407(6804):623-6.
533 4. Timmers PHA, Welte CU, Koehorst JJ, Plugge CM, Jetten MSM, Stams AJM. Reverse
534 methanogenesis and respiration in methanotrophic archaea. Archaea. 2017.
535 5. Chadwick GL, Skennerton CT, Laso-Pérez R, Leu AO, Speth DR, Yu H, et al.
536 Comparative genomics reveals electron transfer and syntrophic mechanisms differentiating
537 methanotrophic and methanogenic archaea. PLoS Biol. 2022;20(1).
538 6. Wang Y, Wegener G, Ruff SE, Wang F. Methyl/alkyl-coenzyme M reductase-based
539 anaerobic alkane oxidation in archaea. Environ Microbiol. 2021;23(2):530-41.
540 7. Wegener G, Krukenberg V, Ruff SE, Kellermann MY, Knittel K. Metabolic capabilities
541 of microorganisms involved in and associated with the anaerobic oxidation of methane. Front
542 Microbiol. 2016;7.
543 8. Wegener G, Krukenberg V, Riedel D, Tegetmeyer HE, Boetius A. Intercellular wiring
544 enables electron transfer between methanotrophic archaea and bacteria. Nature.
545 2015;526(7574):587-90.
546 9. Schnakenberg A, Aromokeye DA, Kulkarni A, Maier L, Wunder LC, Richter-
547 Heitmann T, et al. Electron acceptor availability shapes anaerobically methane-oxidizing
548 archaea (ANME) communities in South Georgia sediments. Front Microbiol. 2021;12:617280.

549 10. Raghoebarsing AA, Pol A, van de Pas-Schoonen KT, Smolders AJP, Ettwig KF,
550 Rijpstra WIC, et al. A microbial consortium couples anaerobic methane oxidation to
551 denitrification. Nature. 2006;440(7086):918-21.
552 11. Ouboter HT, Mesman R, Sleutels T, Postma J, Wissink M, Jetten MSM, et al.
553 Mechanisms of extracellular electron transfer in anaerobic methanotrophic archaea. Nat
554 Commun. 2024;15(1):1477.
555 12. Nauhaus K, Albrecht M, Elvert M, Boetius A, Widdel F. *In vitro* cell growth of marine
556 archaeal-bacterial consortia during anaerobic oxidation of methane with sulfate. Environ
557 Microbiol. 2007;9(1):187-96.
558 13. Holler T, Widdel F, Knittel K, Amann R, Kellermann MY, Hinrichs KU, et al.
559 Thermophilic anaerobic oxidation of methane by marine microbial consortia. ISME J.
560 2011;5(12):1946-56.
561 14. Vaksmaa A, Guerrero-Cruz S, van Alen TA, Cremers G, Ettwig KF, Lüke C, et al.
562 Enrichment of anaerobic nitrate-dependent methanotrophic '*Candidatus* Methanoperedens
563 nitroreducens' archaea from an Italian paddy field soil. Appl Microbiol Biotechnol.
564 2017;101(18):7075-84.
565 15. Krüger M, Meyerdierks A, Glöckner FO, Amann R, Widdel F, Kube M, et al. A
566 conspicuous nickel protein in microbial mats that oxidize methane anaerobically. Nature.
567 2003;426(6968):878-81.
568 16. Lemaire ON, Wagner T. A structural view of alkyl-coenzyme M reductases, the first
569 step of alkane anaerobic oxidation catalyzed by archaea. Biochemistry. 2022;61(10):805-21.
570 17. Thauer RK. Methyl (alkyl)-coenzyme M reductases: Nickel F-430-containing enzymes
571 involved in anaerobic methane formation and in anaerobic oxidation of methane or of short
572 chain alkanes. Biochemistry. 2019;58(52):5198-220.
573 18. Scheller S, Goenrich M, Boecher R, Thauer RK, Jaun B. The key nickel enzyme of
574 methanogenesis catalyses the anaerobic oxidation of methane. Nature. 2010;465(7298):606-
575 U97.
576 19. Mayr S, Latkoczy C, Krüger M, Günther D, Shima S, Thauer RK, et al. Structure of an
577 F_{430} variant from archaea associated with anaerobic oxidation of methane. J Am Chem Soc.
578 2008;130(32):10758-67.
579 20. Hahn CJ, Lemaire ON, Kahnt J, Engilberge S, Wegener G, Wagner T. Crystal structure
580 of a key enzyme for anaerobic ethane activation. Science. 2021;373(6550):118-21.

581 21. Nayak DD, Liu AD, Agrawal N, Rodriguez-Carerro R, Dong SH, Mitchell DA, et al.
582 Functional interactions between posttranslationally modified amino acids of methyl-coenzyme
583 M reductase in *Methanosarcina acetivorans*. PLoS Biol. 2020;18(2).
584 22. Nayak DD, Mahanta N, Mitchell DA, Metcalf WW. Post-translational thioamidation of
585 methyl-coenzyme M reductase, a key enzyme in methanogenic and methanotrophic Archaea.
586 eLife. 2017;6.
587 23. Deobald D, Adrian L, Schöne C, Rother M, Layers G. Identification of a unique radical
588 SAM methyltransferase required for the sp^3-C-methylation of an arginine residue of methyl-
589 coenzyme M reductase. Sci Rep. 2018;8.
590 24. Chen H, Gan QL, Fan CG. Methyl-coenzyme M reductase and its post-translational
591 modifications. Front Microbiol. 2020;11.
592 25. Shima S, Krueger M, Weinert T, Demmer U, Kahnt J, Thauer RK, et al. Structure of a
593 methyl-coenzyme M reductase from Black Sea mats that oxidize methane anaerobically.
594 Nature. 2012;481(7379):98-101.
595 26. Shao NN, Fan Y, Chou CW, Yavari S, Williams RV, Amster IJ, et al. Expression of
596 divergent methyl/alkyl coenzyme M reductases from uncultured archaea. Commun Biol.
597 2022;5(1).
598 27. Berger S, Frank J, Dalcin Martins P, Jetten MSM, Welte CU. High-quality draft
599 genome sequence of "*Candidatus* Methanoperedens sp." strain BLZ2, a nitrate-reducing
600 anaerobic methane-oxidizing archaeon enriched in an anoxic bioreactor. Genome Announc.
601 2017;5(46).
602 28. Kurth JM, Smit NT, Berger S, Schouten S, Jetten MSM, Welte CU. Anaerobic
603 methanotrophic archaea of the ANME-2d clade feature lipid composition that differs from
604 other ANME archaea. FEMS Microbiol Ecol. 2019;95(7).
605 29. Wissink M, Glodowska M, van der Kolk MR, Jetten MSM, Welte CU. Probing
606 denitrifying anaerobic methane oxidation via antimicrobial intervention: implications for
607 innovative wastewater management. Environ Sci Technol. 2024;58(14):6250-7.
608 30. Berger S, Cabrera-Orefice A, Jetten MSM, Brandt U, Welte CU. Investigation of
609 central energy metabolism-related protein complexes of ANME-2d methanotrophic archaea by
610 complexome profiling. Biochim Biophys Acta Bioenerg. 2021;1862(1):148308.
611 31. Echeveste Medrano MJ, Leu AO, Pabst M, Lin Y, McIlroy SJ, Tyson GW, et al.
612 Osmoregulation in freshwater anaerobic methane-oxidizing archaea under salt stress. ISME J.
613 2024;18(1).

614 32. Kurth JM, Müller M-C, Welte CU, Wagner T. Structural insights into the methane-
615 generating enzyme from a methoxydotrophic methanogen reveal a restrained gallery of post-
616 translational modifications. Microorganisms. 2021;9(4).
617 33. Ohmer CJ, Dasgupta M, Patwardhan A, Bogacz I, Kaminsky C, Doyle MD, et al. XFEL
618 serial crystallography reveals the room temperature structure of methyl-coenzyme M
619 reductase. J Inorg Biochem. 2022;230:111768.
620 34. van Kessel MA, Stultiens K, Slegers MF, Guerrero Cruz S, Jetten MS, Kartal B, et al.
621 Current perspectives on the application of N-damo and anammox in wastewater treatment. Curr
622 Opin Biotechnol. 2018;50:222-7.
623 35. Garcia PS, Gribaldo S, Borrel G. Diversity and evolution of methane-related pathways
624 in Archaea. Annu Rev Microbiol. 2022;76:727-55.
625 36. Kurth JM, Nobu MK, Tamaki H, de Jonge N, Berger S, Jetten MSM, et al.
626 Methanogenic archaea use a bacteria-like methyltransferase system to demethoxylate aromatic
627 compounds. ISME J. 2021;15(12):3549-65.
628 37. Widdel F, Bak F. Gram-negative mesophilic sulfate-reducing bacteria. In: Balows A,
629 Trüper HG, Dworkin M, Harder W, Schleifer K-H, editors. The Prokaryotes: A Handbook on
630 the Biology of Bacteria: Ecophysiology, Isolation, Identification, Applications. New York,
631 NY: Springer New York; 1992. p. 3352-78.
632 38. Laso-Pérez R, Krukenberg V, Musat F, Wegener G. Establishing anaerobic
633 hydrocarbon-degrading enrichment cultures of microorganisms under strictly anoxic
634 conditions. Nat Protoc. 2018;13(6):1310-30.
635 39. Prjibelski A, Antipov D, Meleshko D, Lapidus A, Korobeynikov A. Using SPAdes De
636 Novo Assembler. Curr Protoc Bioinformatics. 2020;70(1):e102.
637 40. Pan S, Zhao XM, Coelho LP. SemiBin2: self-supervised contrastive learning leads to
638 better MAGs for short- and long-read sequencing. Bioinformatics. 2023;39(39 Suppl 1):i21-
639 i9.
640 41. Chaumeil PA, Mussig AJ, Hugenholtz P, Parks DH. GTDB-Tk: a toolkit to classify
641 genomes with the Genome Taxonomy Database. Bioinformatics. 2020;36(6):1925-7.
642 42. Seemann T. Prokka: rapid prokaryotic genome annotation. Bioinformatics.
643 2014;30(14):2068-9.
644 43. Woodcroft BJ, Aroney STN, Zhao R, Cunningham M, Mitchell JAM, Blackall L, et al.
645 SingleM and Sandpiper: Robust microbial taxonomic profiles from metagenomic data.
646 BioRxiv. 2024.

647 44. Edgar RC. MUSCLE: multiple sequence alignment with high accuracy and high
648 throughput. Nucleic Acids Res. 2004;32(5):1792-7.
649 45. Stamatakis A. RAxML version 8: a tool for phylogenetic analysis and post-analysis of
650 large phylogenies. Bioinformatics. 2014;30(9):1312-3.
651 46. Carpentier P, van der Linden P, Mueller-Dieckmann C. The High-Pressure Freezing
652 Laboratory for Macromolecular Crystallography (HPMX), an ancillary tool for the
653 macromolecular crystallography beamlines at the ESRF. Acta Crystallog D. 2024;80(2):80-92.
654 47. Vonrhein C, Flensburg C, Keller P, Sharff A, Smart O, Paciorek W, et al. Data
655 processing and analysis with the *autoPROC* toolbox. Acta Crystallogr D Struct Biol.
656 2011;67:293-302.
657 48. Liebschner D, Afonine PV, Baker ML, Bunkóczi G, Chen VB, Croll TI, et al.
658 Macromolecular structure determination using X-rays, neutrons and electrons: recent
659 developments in *Phenix*. Acta Crystallogr D Struct Biol. 2019;75:861-77.
660 49. Jumper J, Evans R, Pritzel A, Green T, Figurnov M, Ronneberger O, et al. Highly
661 accurate protein structure prediction with AlphaFold. Nature. 2021;596(7873):583-9.
662 50. Emsley P, Lohkamp B, Scott WG, Cowtan K. Features and development of *Coot*. Acta
663 Crystallogr D Biol Crystallogr. 2010;66(Pt 4):486-501.
664 51. Katoh K, Rozewicki J, Yamada KD. MAFFT online service: Multiple sequence
665 alignment, interactive sequence choice and visualization. Brief Bioinform. 2019;20(4):1160-6.
666 52. Robert X, Gouet P. Deciphering key features in protein structures with the new
667 ENDscript server. Nucleic Acids Res. 2014;42(W1):W320-W4.
668 53. Chovancova E, Pavelka A, Benes P, Strnad O, Brezovsky J, Kozlikova B, et al. CAVER
669 3.0: a tool for the analysis of transport pathways in dynamic protein structures. PLoS Comput
670 Biol. 2012;8(10):e1002708.
671

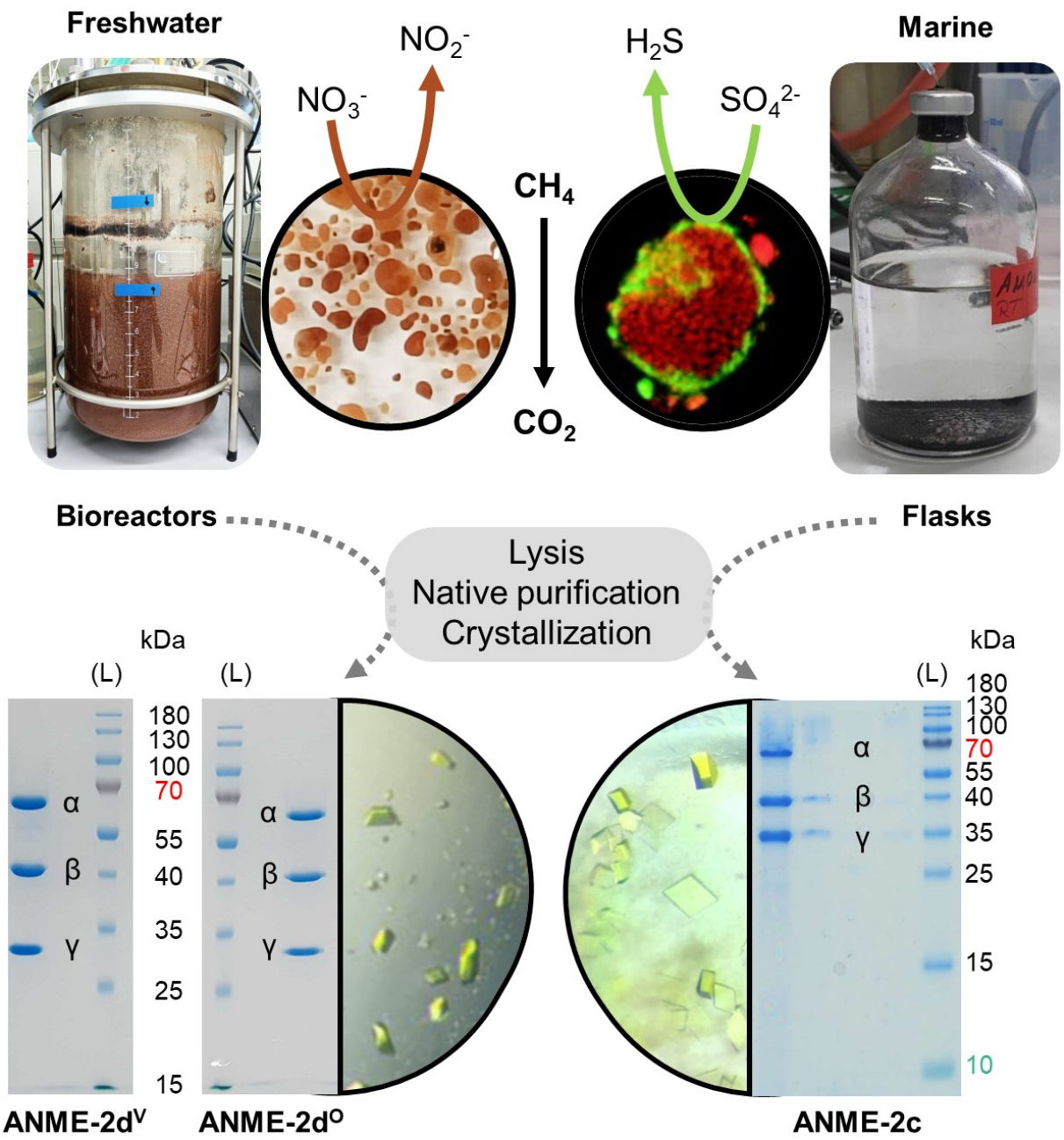

Figure 1. Comparison of the ANME-2 samples investigated in this study and procedure of protein isolation by native purification and crystallisation. Images of the bioreactor and flasks containing the respective freshwater and marine ANME-2 are presented. Close-ups of granular biomass of ANME-2d reducing NO_3^- and fluorescence *in situ* hybridisation labelled micrographs of the marine methanotrophic consortium (red for the archaeon and green for the sulfate-reducing partner, using specific probes) are shown. Biological samples were used to purify the major MCR fraction, as shown on the SDS-PAGE gel at the bottom of the figure. For ANME-2c, the sample passed on SDS-PAGE corresponds to dissolved crystals, and a picture of the purification procedure can be examined in Supplementary Fig. S2. L stands for ladder.

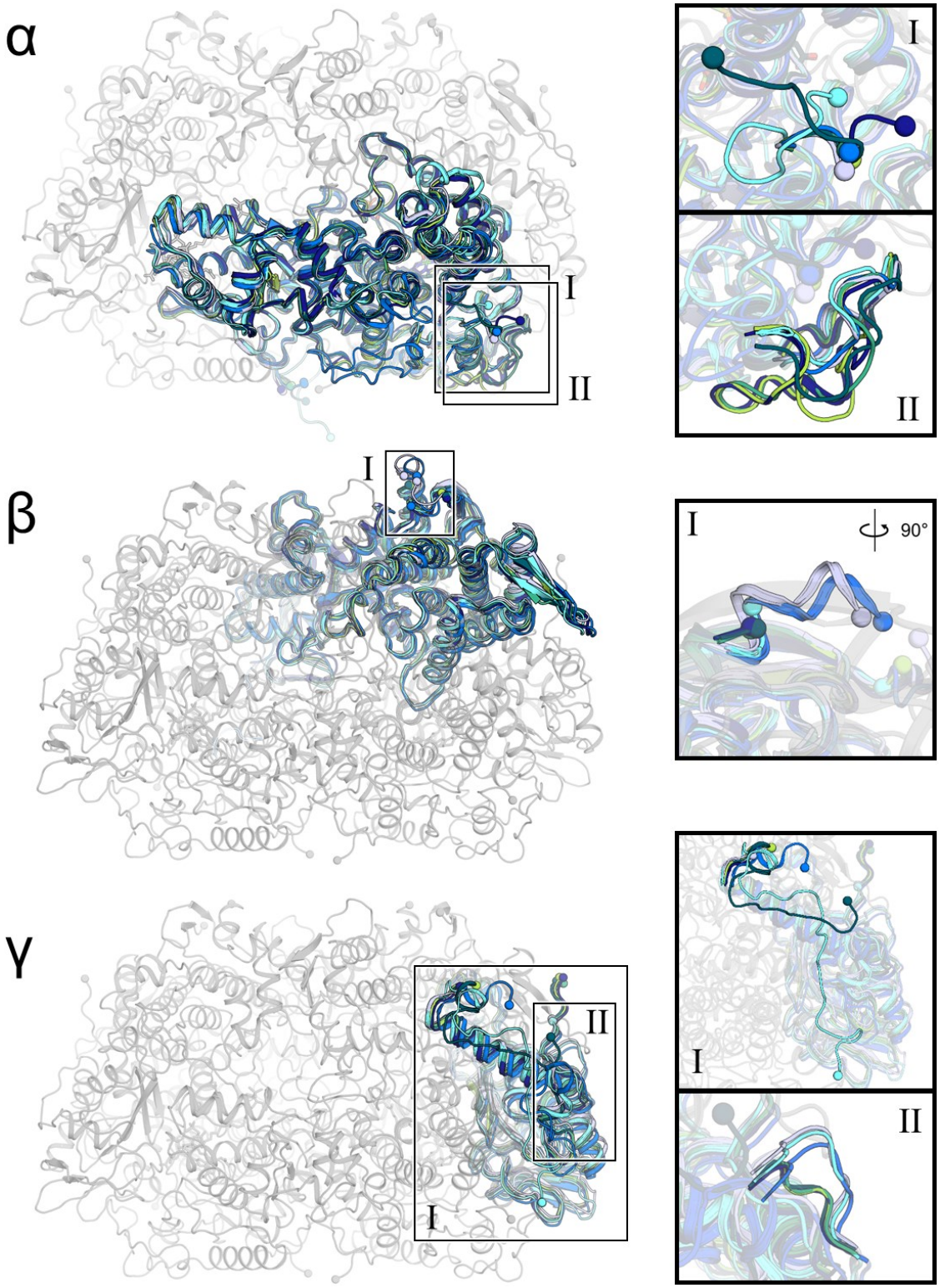

Figure 2. Comparison of ANME-2 MCR structures with previously structurally characterised MCRs. Superposition of the α-, β-, and γ-subunits of MCR. The panels on the right are close-ups of structural deviations. In each panel, the corresponding chain is coloured, while the remaining chains are shown (greyed out) for ANME-2d^{V}. MCR structures are coloured according to the microorganism, with *M. marburgensis* (PDB code: 5A0Y) in light blue, *M. shengliensis* (7NKG) in deep blue, ANME-1 from Black Sea mats (3SQG) in cyan, *Ca.* E. thermophilum ECR (71BS) in marine, ANME-2c in dark green, ANME-2d^{O} in green and ANME-2d^{V} in light green. N- and C-termini are shown as spheres and ligands as sticks.

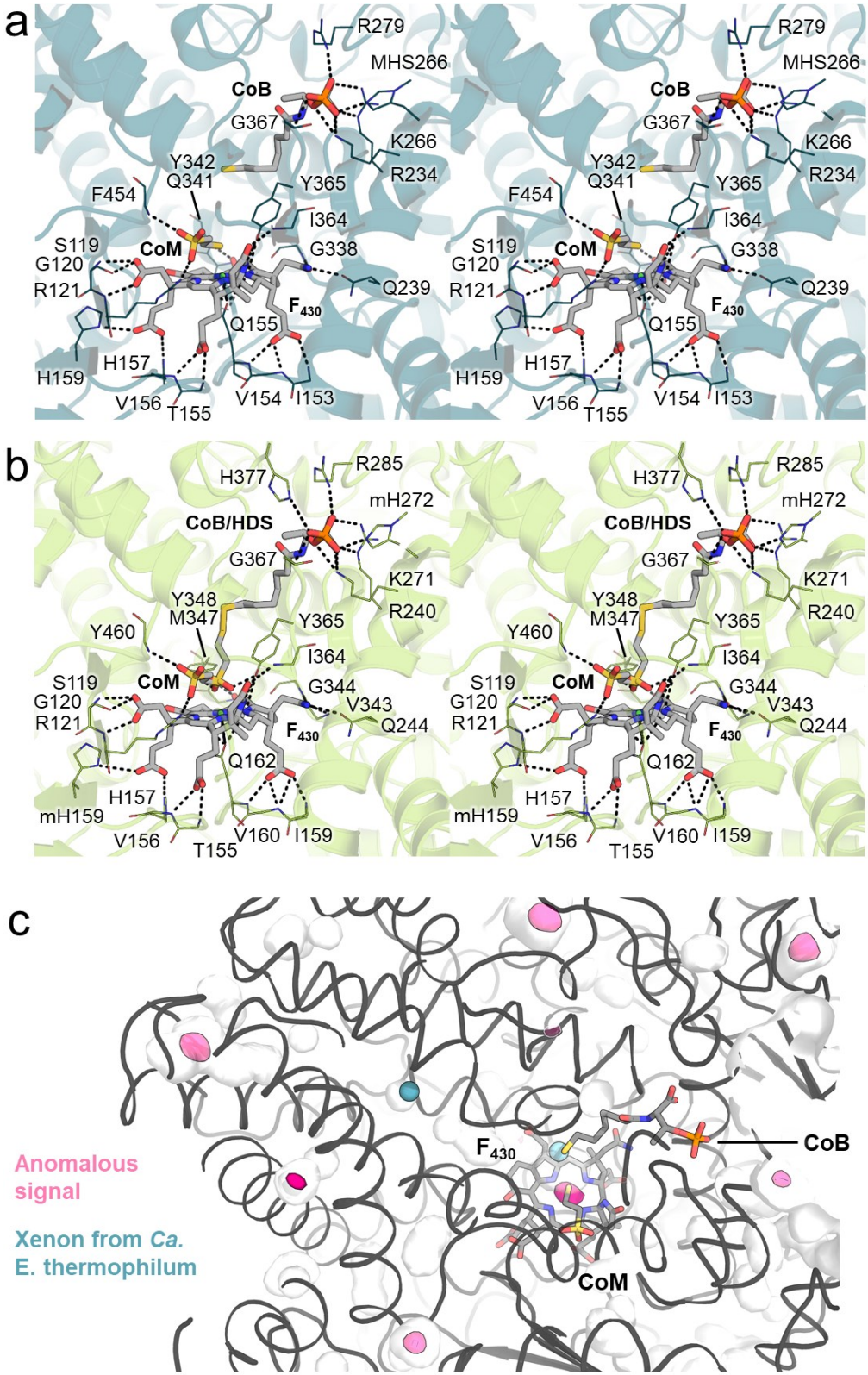

Figure 3. ANME-2 MCR active sites. Stereo-view of the MCR active site in (**a**) ANME-2c and (**b**) ANME-2d^{v}. Coordinating residues are shown as lines, and non-interacting side- or main chains were omitted. Polar contacts are depicted as black dashes. (**c**) Anomalous map for Krypton position shown as pink surfaces and contoured at 5 σ. Xenon position from *Ca*. E. thermophilum are teal spheres. Proteins are in cartoons, and ligands are shown as sticks coloured according to atom (red for O, blue for N, orange for P, yellow for S).

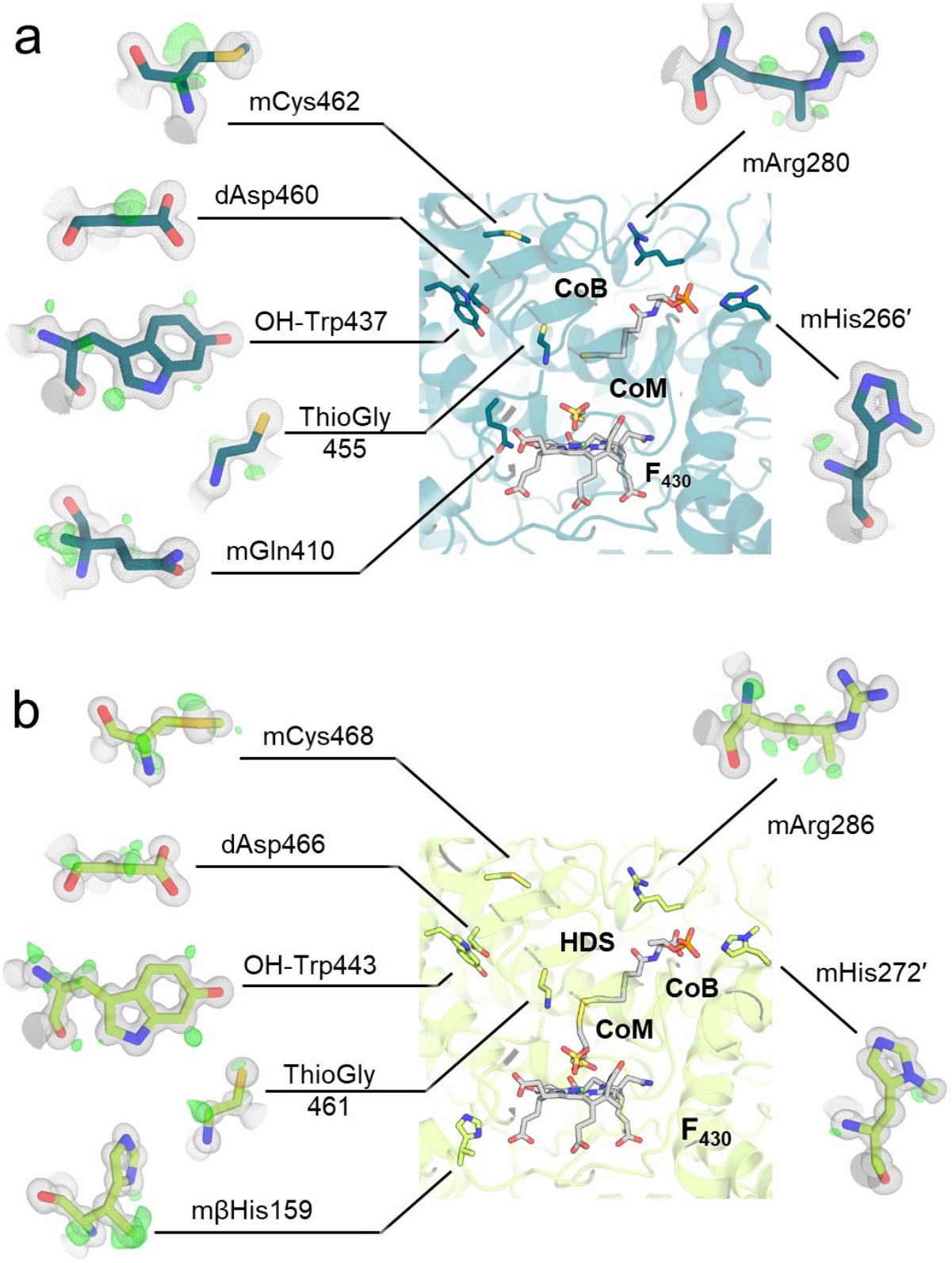

Figure 4. ANME-2 MCR post-translational modifications. PTMs in the active site of (**a**) ANME-2c and (**b**) ANME-2d^{V}. The main chain is shown as a cartoon, with ligands and PTMs shown as sticks coloured according to atom (red for O, blue for N, orange for P, yellow for S). Close-ups of PTMs flank the central picture, highlighting electron densities. The $2F_o{-}F_c$ map (grey mesh) is contoured at 1 σ, and the $F_o{-}F_c$ map (green mesh) is contoured at 3 σ. The latter highlights the experimental hydrogen positions. The 3(*S*)-methylhistidine is on the γ-chain.

707 **Table 1: X-ray analysis statistics for ANME-2 MCR**

	ANME-2c from microbial enrichment	ANME-2c (Kr pressurized)	ANME-2d^{O} from bioreactor	ANME-2d^{V} from bioreactor
Data collection				
Synchrotron and beamline	SOLEIL, PROXIMA-1	ESRF, ID23-1	ESRF, BM07-FIP2	ESRF, BM07-FIP2
Wavelength (Å)	0.97856	0.86100	0.97980	0.97930
Space group	$P2_1$	$P2_12_12_1$	$P2_1$	$P2_1$
Resolution (Å)	127.16 – 1.34 (1.50 – 1.34)	59.40 – 1.80 (1.83 – 1.80)	76.67 – 0.98 (1.04 − 0.98)	96.94 – 0.92 (1.04 − 0.92)
Cell dimensions				
a, b, c (Å)	156.87, 157.46, 215.42	153.48, 153.67, 212.88	81.58, 189.30, 84.11	81.64, 189.89, 83.96
α, β, γ (°)	90, 90.34, 90	90, 90, 90	90, 114.27, 90	90, 114.36, 90
R_{merge} (%)[a]	16.8 (167.1)	12.7 (162.3)	11.9 (116.8)	6.8 (96.2)
R_{pim} (%)[a]	7.3 (73.7)	5.1 (64.6)	4.5 (46.8)	2.6 (38.1)
$CC_{1/2}$ [a]	0.991 (0.560)	0.999 (0.768)	0.996 (0.667)	0.998 (0.684)
I/σ_I[a]	6.6 (1.6)	14.1 (1.8)	9.4 (1.7)	13.0 (1.7)
Spherical completeness[a]	66.2 (12.2)	/	84.4 (24.4)	62.6 (10.4)
Ellipsoidal completeness[a]	96.2 (66.6)	100.0 (100.0)	96.5 (70.9)	84.7 (58.5)
Redundancy[a]	6.3 (6.0)	13.8 (14.2)	7.8 (7.1)	7.6 (7.2)
Nr. unique reflections[a]	1,527,343 (76,367)	461,593 (22,707)	1,130,261 (56,513)	988,467 (49,423)
Refinement				
Resolution (Å)	98.93 – 1.34		41.78 – 0.98	41.72 – 0.94
Number of reflections	1,527,209		1,130,120	986,474
R_{work}/R_{free}[b] (%)	11.30/14.81		10.32/11.90	11.21/13.06
Number of atoms				
Protein	152,083		38,640	38,408
Ligands/ions	912		283	289
Solvent	9452		3203	3,075
Mean B-value (Å^2)	15.86		10.40	11.95
Molprobity clash score	1.28		1.42	1.18
Ramachandran plot				
Favoured regions (%)	97.31		97.16	97.08
Outlier regions (%)	0.07		0.08	0.12
rmsd[c] bond lengths (Å)	0.010		0.010	0.010
rmsd[c] bond angles (°)	1.235		1.298	1.321

708 [a] Values relative to the highest resolution shell are within parentheses. [b] Rfree was calculated
709 as the Rwork for 5 % of the reflections that were not included in the refinement. [c] rmsd, root
710 mean square deviation.

711